Structural dependence of electric field gradients in $Pb(Zr_{1-x}Ti_x)O_3$ from first principles

Dandan Mao, Eric J. Walter, and Henry Krakauer*
Department of Physics, College of William and Mary, Williamsburg, Virginia, 23187-8795, USA

Zhigang Wu
Computational Nanoscience Group, University of California at Berkeley, Berkeley, California, 94720, USA
(Received 13 April 2007; revised manuscript received 1 June 2007; published 12 July 2007)

First-principles all-electron density functional theory calculations of electric field gradients (EFGs) are presented for $PbTiO_3$ and structural models of $Pb(Zr_{1/2}Ti_{1/2})O_3$. Calculations were carried out as a function of *B*-site chemical ordering, applied strain, and imposed symmetry. Large changes in the EFGs are seen as the electric polarization rotates between the tetragonal and monoclinic structures. The onset of polarization rotation in *Cm* symmetry strongly correlates with the shearing of the TiO_6 octahedra, and there is a sharp change in slope in plots of Ti EFGs vs octahedral distortion index. Trends in the calculated oxygen EFGs are consistent with recent nuclear magnetic resonance (NMR) measurements, which indicate significant sensitivity of oxygen NMR peaks to changes in the local structure as a function of Ti concentration. Calculated Ti EFGs are considerably larger than those inferred from the NMR measurements. Based on comparisons with experiment, the calculated results are interpreted in terms of static and dynamic structural models of $Pb(Zr_{1-x}Ti_x)O_3$.

DOI: 10.1103/PhysRevB.76.014105 PACS number(s): 77.84.Dy, 71.15.Mb, 77.84.−s, 76.60.Gv

I. INTRODUCTION

Due to their excellent piezoelectric, ferroelectric, and dielectric properties, Pb based complex ferroelectric alloys have been widely used in various technical applications, such as sensors, capacitors, memory applications, actuators, and transducers.[1–4] The piezoelectric response of these disordered alloys depends on their composition and possibly local atomic ordering.[2,5,6] Experimental probes of local structural properties include x-ray absorption fine structure spectroscopy, neutron scattering pair distribution function measurements,[7] and high field NMR techniques.[8]

Recently, high field NMR measurements have shown great promise as a probe of the local structure of ABO_3 perovskite-based alloys by their ability to resolve line broadening of NMR spectra due to the nuclear quadrupolar coupling (for nuclei with spin $I>1/2$) with the electric field gradient (EFG) at the nucleus. Since the EFG at a nucleus is sensitive to local changes in electronic density, its effect on NMR spectra can serve as a useful probe of local atomic structure. For example, high field NMR magic angle spinning ^{93}Nb spectra were recently presented for solid solutions of $(1-x)Pb(Mg_{1/3}Nb_{2/3})O_3+xPb(Sc_{1/2}Nb_{1/2})O_3$,[8] where distinct peaks were assigned according to the percentages of Mg, Sc, and Nb occupying the six nearest *B* sites of the Nb atoms. NMR measurements of Ti-EFGs in $BaTiO_3$ have recently been used to argue for the coexistence of order-disorder and displacive components in the phase transition mechanism.[9] For a given nuclear isotope, each chemically inequivalent site produces its own EFG-induced NMR line shifts and broadenings. In addition, each chemically inequivalent site will, in general, be subject to different chemical shifts of the NMR spectra due to screening of the applied magnetic field by induced electronic currents.[10] The combination of these effects can make it difficult to discriminate spectra arising from inequivalent sites. It is thus of considerable interest to provide theoretical guidance to interpret these spectra. In this paper, we describe calculations of EFG-related effects on NMR spectra.

All-electron first-principles approaches such as the linearized augmented plane wave (LAPW) method are usually used to calculate EFGs.[11–17] The difficulty with widely used pseudopotential methods is the incorrect form of the pseudo-wave-functions near the atomic nuclei. Pseudo-wave-functions lack the nodal features of the true valence wave functions, which arise from orthogonality of the latter to the core-electron states, which are absent in a pseudopotential calculation. This can result in sizable errors, since the EFG depends sensitively on the charge density near the nucleus. Recently, EFGs have been successfully calculated using the projector augmented wave (PAW) method.[18] While the PAW method is sometimes regarded as a plane wave pseudopotential approach, it is essentially an all-electron method that retains the correct nodal properties of the valence wave functions near the nucleus. First-principles methods have been applied successfully to many materials.[11–18] First-principles all-electron methods are thus a reliable means to determine EFGs in perovskite alloys.

$Pb(Zr_{1-x}Ti_x)O_3$ (PZT) is a well-studied ferroelectric material whose *B* site is randomly occupied by either a Zr or Ti cation. Below 250 °C and below 7% Ti, PZT is antiferroelectric; however, it becomes ferroelectric as the concentration of Ti increases above 7%. An almost vertical morphotropic phase boundary (MPB) at $x=0.52$ separates the Zr-rich rhombohedral phase from the Ti-rich tetragonal phase, and large piezoelectric coupling occurs for compositions near the MPB. Noheda *et al.* discovered a monoclinic phase in PZT at low temperatures in a narrow compositional range at the MPB.[19] Polarization rotation has been proposed as the origin of the large piezoelectric response in PZT and related materials. The polarization rotation mechanism was proposed by Park and Shrout to explain the giant piezoelectric response in single-crystal piezoelectrics $(1-x)Pb(Zn_{1/3}Nb_{2/3})O_3+xPbTiO_3$ (PZN-PT) and $(1-x)Pb(Mg_{1/3}Nb_{2/3})O_3$

$+x$PbTiO$_3$ PMN-PT.[4] Using first-principles calculations, Fu and Cohen[20] found that large strain response is induced in $BaTiO_3$ by polarization rotation induced by a noncollinear applied electric field, while the strain response for collinear applied field was much smaller. They calculated a strain vs field curve that was qualitatively similar to that observed in PZN-8%PT.[4] The new monoclinic phase near the MPB of PZT suggested that the new phase might serve as a bridge between the tetragonal and rhombohedral phases.[19] Subsequent effective Hamiltonian calculations by Bellaiche *et al.*[21] also showed this behavior. Wu and Krakauer[22] performed direct first-principles calculations of the piezoelectric response in PZT 50/50 and found greatly enhanced piezoelectric coefficients due to polarization rotation as a function of applied strain in the monoclinic phase. Similar polarization rotation has been observed in related materials such as PZN-8%PT[23] via an orthorhombic intermediate phase, and the existence of such intermediate phases has been established on general principles by Vanderbilt and Cohen.[24] Dmowski *et al.*[7] examined the local structure for PZT compositions near the MPB using atomic pair distribution functions (PDFs) obtained from Fourier transform of the neutron scattering structure factor. Based on comparisons with model PDFs, they found that the greatest change with varying Ti/Zr composition was the distribution in direction of the Pb displacements, with Ti-rich local environments tending to have $\langle 100 \rangle$ pseudocubic Pb displacements while Zr-rich environments tending to have $\langle 110 \rangle$ pseudocubic Pb displacements.

Recently, Baldwin *et al.*[25] presented an NMR solid-state study of PZT solid-solution series as a function of x using ^{17}O, ^{47,49}Ti, and ^{207}Pb spectra. They interpreted their results as providing evidence for an anisotropy in the local structure of PZT solutions. In this paper, we calculate EFGs in PZT structures as a function of chemical ordering and applied strain to assess this interpretation.

The paper is organized as follows. In Sec. II, we give technical details of the LAPW evaluation of EFGs. Section III describes the PZT structural models and compares the relaxed structures with experimental pair distribution measurements. In Sec. IV, we present EFG results and calculated NMR EFG powder spectra as a function of chemical ordering and strain. A discussion of our results and comparison with recent PZT NMR measurements are given in Sec. V, and Sec. VI summarizes our results.

II. METHODOLOGY

All calculations were performed with the local density approximation (LDA) using the first-principles all-electron LAPW plus local orbital method.[26] The local orbital extension yields the most accurate treatment of atoms with extended semicore orbitals, allowing them to be treated variationally along with the valence bands in a single energy window. The use of local orbitals can also provide additional variational freedom for valence states. Local orbitals were associated with the Zr $4s$, $4p$, Ti $3s$, $3p$, and O $2s$, $2p$ states. Core-electron states were calculated with a fully relativistic atomiclike approximation using the self-consistent crystal potential. The valence states were treated scalar relativistically, and the Hedin-Lundqvist exchange-correlation functional[27] was used. The LAPW basis functions, charge density, and potential are all described by a dual representation. Within nonoverlapping ("muffin-tin") spheres that are centered on the nuclear positions, these functions are represented by numerical radial functions times spherical harmonics. In the interstitial region between the spheres, all functions are represented by plane wave expansions. Muffin-tin (MT) sphere radii of 2.30, 1.65, 1.65, and 1.55 a.u. were used for the Pb, Zr, Ti, and O ions, respectively. For all systems, a well-converged 44 Ry plane wave energy cutoff was used, and special **k** points[28] were used to sample the Brillouin zone with a $4\times4\times4$ mesh.

In a crystal, the EFG at an atomic nucleus is induced by the nonspherical field of the electrons and other ions. Typically, the dominant electronic contributions come from the valence electron and shallow semicore states. Ehmann and Fahnle[29] have calculated EFG corrections due to the polarization of tightly bound core-electron states using a method similar to Sternheimer's.[30] In their calculations, the perturbation acting on the core states is due to the nonspherical effective crystal potential near the nucleus, as determined from first-principles all-electron LAPW calculations using a spherical core. For a nearest-neighbor site of a substitutional Ni atom in Cu, they found that the principal core contributions to the Cu EFG came from the Cu($3p$) states, about 25% of the calculated EFG using spherical core states, while the contributions of the $2p$ states was small and the s-state contributions could be neglected. In the present calculations, the corresponding Ti($3s$,$3p$) and Zr($4s$,$4p$) shells are treated variationally, and so the effects of core polarization are adequately treated.

The EFG at a nuclear position is a symmetric traceless tensor defined as[31]

$$V_{ij} = \lim_{r\to 0}\left(\frac{\partial^2 V(\mathbf{r})}{\partial r_i \partial r_j} - \frac{1}{3}\delta_{ij}\nabla^2 V\right), \tag{1}$$

where $V(\boldsymbol{r})$ is the Coulomb potential. The three eigenvalues of the EFG tensor are its components V_{zz}, V_{yy}, and V_{xx} with respect to the principal axis x-y-z frame defined by the corresponding eigenvectors. In conventional notation, the eigenvalues are ordered such that $|V_{zz}|>|V_{yy}|>|V_{xx}|$. Since the EFG tensor is traceless, these can be expressed in terms of two independent variables, V_{zz} and the asymmetry parameter $\eta=(V_{xx}-V_{yy})/V_{zz}$, where $0\leqslant\eta\leqslant1$. Simulated NMR EFG powder spectra are also reported below, corresponding to the second-order central transition $(m=1/2\leftrightarrow-1/2)$ $\nu_{1/2}^{(2)}$ of the half-integral nuclear spin atoms considered in this paper (see, for example, Refs. 10 and 31). NMR hyperfine levels calculated using perturbation theory to treat the EFG quadrupolar interaction were checked by exact diagonalization of the Hamiltonian in the $(2m+1)$-dimensional I subspace.[32] The resulting powder patterns were virtually identical for the high (18 T) magnetic fields used in the calculations.

For each structure, all the atomic positions were allowed to relax, consistent with the imposed symmetry, until the calculated forces were less than 0.02 eV/Å. We estimate that

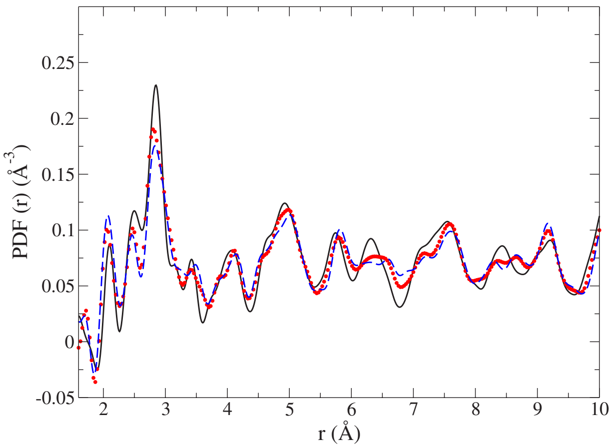

FIG. 1. (Color online) PZT experimental 10 K pair distribution functions (PDF) from Fig. 4 of Dmowski *et al.* (Ref. 7): 60% Ti with average *P*4*mm* symmetry (solid line), 48% Ti with average *Cm* symmetry [(red) dotted line], and 40% Ti with average *R*3*c* symmetry [(blue) dashed line].

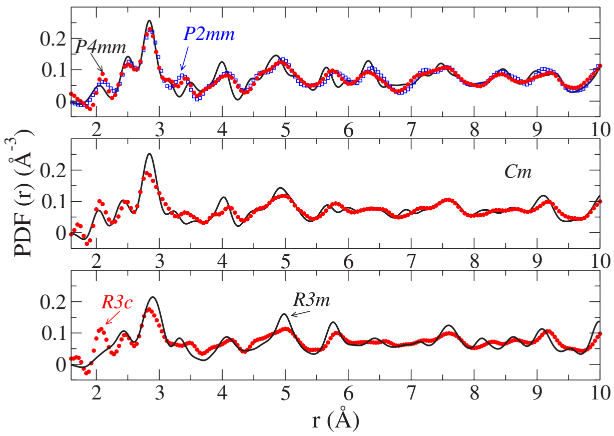

FIG. 2. (Color online) PZT 10 K experimental pair distribution functions (PDF) [(red) dotted curves] from Dmowski *et al.* (Ref. 7) are compared to simulated PDFs, calculated using the relaxed atomic positions (see text). Top panel: experimental PDF for 60% Ti with average *P*4*mm* symmetry and calculated PZT 50/50 PDFs with symmetries *P*4*mm* (solid line) and *P*2*mm* [(blue) box symbols]. Middle panel: experimental PDF for 48% Ti with average *Cm* symmetry and calculated PZT 50/50 PDF with *Cm* symmetry (solid line). Bottom panel: experimental PDF for 40% Ti with average *R*3*c* symmetry and calculated PZT 50/50 PDF with *R*3*m* symmetry (solid line).

the resulting EFGs are accurate to less than ~5% error with respect to the atomic positions.

III. STRUCTURAL MODELS AND COMPARISON WITH EXPERIMENTAL PAIR DISTRIBUTION FUNCTIONS

PZT 50/50 was studied using ten atom supercells. Most of the calculations were performed for [001]1:1 *B*-site ordered unit cells, with the ferroelectric polarization direction along the [001] axis in imposed *P*4*mm* symmetry. This corresponds to alternating Zr and Ti atoms along the [001] direction. In this structure, the *B*-atom planes perpendicular to the [001] direction contain either all Zr or all Ti. Calculations with these supercells were performed for various c/a values with imposed tetragonal *P*4*mm*, monoclinic *Cm*, and *P*1 triclinic symmetry. Experimentally, Noheda *et al.*[19] find that monoclinic PZT, near 50/50 composition, has only a small monoclinic angular distortion β of 90.5°. In our calculations, we simply set this angle to 90° in all of our calculations. Some calculations were also performed for supercells with [001]1:1 *B*-site ordering with imposed orthorhombic *P*2*mm* symmetry. The *P*2*mm* orthorhombic unit cell has dimensions $a' \times a \times 2a$, corresponding to alternating Ti and Zr *B*-atom stacking along the [001] direction with periodicity 2*a*, with the ferroelectric polarization along the a' [100] direction. Thus, the *P*2*mm* c/a value given in Table II is actually $a'/a=1.04$. Finally, we also studied a [111]1:1 *B*-site ordered supercell with imposed *R*3*m* symmetry. In all calculations, the unit cell was set to the experimental volume.[33]

The relaxed structural models can be compared to experimentally determined pair distribution functions. Experimental 10 K PDFs from Dmowski *et al.*[7] (their Fig. 4) are shown in Fig. 1. The experimental PDFs were obtained from Fourier transform of neutron scattering structure factors. The average observed symmetry is tetragonal *P*4*mm* for 60% Ti, monoclinic *Cm* for 48% Ti, and rhombohedral *R*3*c* for 40% Ti. Figure 2 compares the calculated PDFs for the relaxed PZT 50/50 structures with experiment. The top panel of Fig. 2 compares the experimental 60% Ti PDFs with calculated PDFs for tetragonal *P*4*mm* and also with reduced orthorhombic *P*2*mm* imposed symmetry, the middle panel compares the experimental 48% Ti PDF with the calculated PDF for monoclinic *Cm* imposed symmetry, and the bottom panel compares the experimental 40% Ti with the calculated PDF for rhombohedral *R*3*m* imposed symmetry. The calculations used $c/a=1.045$ (1.02) for *P*4*mm* (*Cm*), respectively, as determined by the experimental Rietveld analysis[7] for the corresponding samples. *P*2*mm* calculations were for $c/a=1.04$. The simulated PDFs were obtained using our calculated relaxed atomic positions as input into the PDFFIT program,[34] which weights pairs of atoms by the product of their neutron scattering lengths. The simulations used $Q_{max}=80$ Å^{-1}, and an isotropic thermal factor of 0.005 Å^2 for all the atoms. Compared to the PZT 40/60 experimental PDF, the rms errors between 1.7 and 10 Å are 0.018 and 0.011 Å^{-3} for *P*4*mm* and *P*2*mm* imposed symmetries, respectively. The rms error for *Cm* symmetry is 0.017 Å^{-3} and 0.022 Å^{-3} for *R*3*m* symmetry.

A generic feature of many lead-based perovskite alloys is the wide range of Pb-O nearest-neighbor bond lengths. Table I shows the Pb-O nearest-neighbor bond lengths in both tetragonal and monoclinic imposed symmetries for the relaxed structures. In tetragonal symmetry, there are four groupings of Pb-O bond lengths: ~2.5, 2.9, 3.2, and 3.5 Å. In imposed monoclinic *Cm* symmetry, the Pb-O groupings are more spread out. The experimental and theoretical curves in the top panel of Fig. 2 both show peaks at ~2.5 2.5, 2.9, and 3.5 Å and a shoulder at ~3.2 Å, corresponding to these Pb-O distances. These features, especially the peak near ~2.5 Å, are also evident at the other compositions. The presence of the 2.5 Å bond length, similar to the shortest Pb-O

TABLE I. Calculated PZT 50/50 Pb-O nearest-neighbor distances (Å) for *Cm* monoclinic and *P*4*mm* tetragonal imposed symmetries. c/a values correspond to Fig. 2, and *m* refers to the number of bonds of the given length.

Cm $c/a=1.02$				*P*4*mm* $c/a=1.045$			
Pb_1-O	*m*	Pb_2-O	*m*	Pb_1-O	*m*	Pb_2-O	*m*
2.437	2	2.384	2	2.533	4	2.484	4
2.515	1	2.496	1	2.871	4	2.877	4
2.816	2	2.757	2	3.170	4	3.535	4
2.901	2	2.906	2				
2.920	2	3.255	2				
3.242	1	3.266	1				
3.248	2	3.533	2				

distance in $PbTiO_3$, is characteristic of PZT and many other perovksite lead-based alloys, as noted by Dmowski *et al.* Based on comparisons with model PDFs, Dmowski *et al.* concluded that the greatest changes with varying Ti/Zr composition in PZT was the distribution in direction of the Pb displacements, with Ti-rich local environments tending to have ⟨100⟩ pseudocubic Pb displacements while Zr-rich environments tended to have ⟨110⟩ pseudocubic Pb displacements. This is consistent with our monoclinic *Cm* calculations, which show that the Pb atoms move toward one side of the oxygen octahedra and displace between the ⟨111⟩ and ⟨001⟩ directions.

Very small energy differences separate the simulated [001]1:1 *B*-site ordered PZT 50/50 *P*2*mm*, *Cm*, and *P*4*mm* relaxed structures shown in Fig. 2. The *P*2*mm* and *Cm* structures differ by only ~0.02 mRy per perovskite formula unit, while the *P*4*mm* structure is only ~1.2 mRy higher in energy. The [111]1:1 *B*-site ordered *R*3*m* structure is the lowest energy structure considered here, being ~23 mRy lower than the [001]1:1 structures. Since ordered PZT does not exist at these compositions, it is likely that the Born-Oppenheimer energy landscape is described by many local minima with small energy separations and with local atomic structure similar to the present [001]1:1 and [111]1:1 models. The system is thus kinetically trapped in a disordered state. However, the good agreement of the calculated PDFs with experiment indicates that the nearest-neighbor atomic structure is reasonably well reproduced in our relaxed structural models.

IV. ELECTRIC FIELD GRADIENT RESULTS AND SIMULATED NMR SPECTRA

Figure 3 displays calculated values of V_{zz} for [001]1:1 ordered PZT, with imposed monoclinic *Cm* and tetragonal *P*4*mm* symmetries, as a function of c/a. For *Cm* symmetry, the corresponding EFG asymmetry parameter η is shown in Fig. 4. The labeling of the atoms is as follows. The Pb_1 and Pb_2 atoms have the shortest $A-B$ bond length with the Zr (Ti) atoms, respectively. For example, at $c/a=1.035$ and with *Cm* symmetry, the Pb_1-*B* distances are 6.34 a.u. (6.64 a.u.) for Zr (Ti), respectively, and Pb_2-*B* distances are 6.82 a.u. (6.17 a.u.) for Zr (Ti), respectively. The ideal $A-B$ bond length at this c/a is 6.66 a.u. Apex (*c*-axis) oxygen atoms O_1 and O_3 have their shortest $B-O$ bond length with the Zr (Ti) atoms, respectively. The O_2 and O_4 atoms are roughly coplanar with the [001] layers of Zr (Ti), respectively.

The rotation of the polarization away from the [001] direction with decreasing c/a is responsible for the abrupt sign change of V_{zz} for the apex oxygen atoms in Fig. 3 for *Cm* symmetry. Polarization rotation also accounts for the increasing Pb V_{zz}. Neither of these features are seen in *P*4*mm* symmetry, where the polarization is constrained to lie along the [001] direction. The polarization rotation coincides with a rotation and shearing of the BO_6 octrahedra, as discussed further below and in Sec. V.

Numerical results for selected c/a are given in Table II. Also shown in the Table II are results for [001]1:1 orthorhombic *P*2*mm* symmetry and triclinic *P*1 symmetry. For

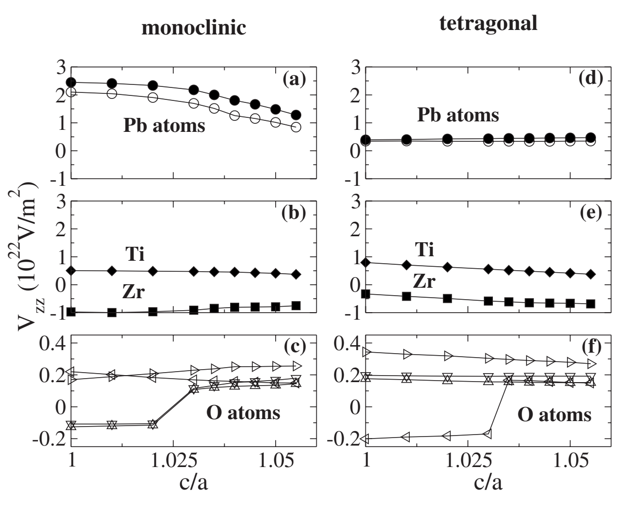

FIG. 3. Calculated V_{zz} vs c/a for PZT (50/50). Panels (a)–(c) are for imposed monoclinic *Cm* symmetry, and panels (d)–(f) are for tetragonal *P*4*mm* symmetry. In (a) and (d), open (filled) circles represent Pb_1 (Pb_2), respectively (see text). In (b) and (e), squares (diamonds) represent Zr (Ti), respectively. In (c) and (f), triangles pointing up, down, left, and right represent oxygen atoms O_1, O_3, O_2, and O_4, respectively (see text). Note the change of scale for the O atoms.

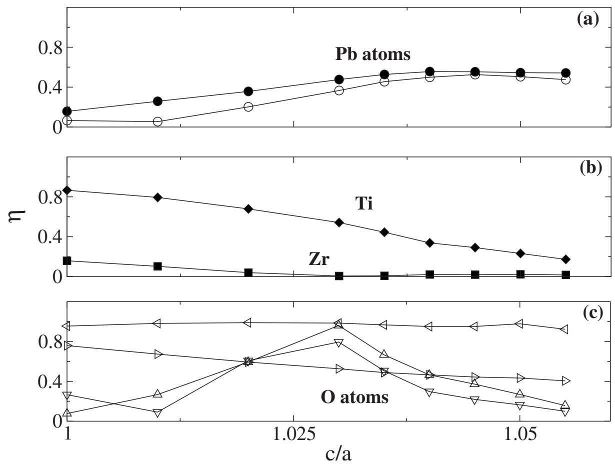

FIG. 4. Calculated EFG asymmetry for PZT (50/50) with imposed monoclinic *Cm* symmetry. Panels (a)–(c) show η vs c/a. Symbols are the same as in Fig. 3.

comparison, EFGs for ground state tetragonal $PbTiO_3$ are shown in Table III, which also shows differences in the calculated EFGs due to differences between calculated and experimental geometries. The large η's of the coplanar O_2 and O_4 atoms seen in the tables can be understood by considering the simpler case of *P*4*mm* symmetry. In both PZT and $PbTiO_3$, the EFG tensor of the coplanar-O atoms have their principal axes oriented as follows. One is along the *c* direction (the ferroelectric distortion direction), one is approximately along the $B-$O bond direction, and the third is perpendicular to these two. The electric field gradients along the *c* and $B-$O bond directions are larger than that perpendicular to the bond due to the B-atom off centering, and this results in large values of η.

Several features are worth noting in the calculated EFGs. As shown by Wu and Krakauer[22] for [001]1:1 ordered PZT with imposed *Cm* symmetry, the electric polarization is nearly parallel to the [001] (*c* axis) for $c/a \gtrsim 1.04$, and it begins to rotate away from the *c* axis at $c/a \sim 1.035$. As seen in Figs. 3 and 4, however, even above $c/a = 1.04$, the EFGs are sensitive to the onset of the polarization rotation. As the electric polarization begins to rotate away from the [001] direction into the *Cm* mirror plane near $c/a \simeq 1.035$, there are large changes in the calculated η's. The η's for Pb and Ti do not vanish even for large c/a values (as they would for imposed *P*4*mm* symmetry). As c/a decreases, η(Pb) decreases while η(Ti) increases. At the same time, the apex oxygen's $\eta(O_1)$ and $\eta(O_3)$ first sharply increase and then decrease as c/a is further reduced. The $\eta(O_4)$, which is coplanar with the Ti, increases monotonically with η(Ti), while η(Zr) and the coplanar $\eta(O_2)$ both stay nearly constant. The η(Zr) is very small, while $\eta(O_2) \simeq 0.95$ is large and about the same as in *P*4*mm* symmetry (not shown in the figure, but see Table II). The structural dependences of the Ti and apex O EFGs are related to the shearing of the TiO_6 octahedra, which is further discussed in Sec. V.

The calculated Pb EFGs show large sensitivity to the structure. For example, near $c/a \simeq 1.035$ in Fig. 3, V_{zz}(Pb) is much larger in *Cm* than in imposed *P*4*mm* symmetry, even though the *Cm* electric polarization is still nearly parallel to the *c* axis. This is also seen in Table II, comparing V_{zz}(Pb) for different imposed symmetries. Upon relaxing the imposed symmetry from monoclinic *Cm* to triclinic *P*1, the Pb-O distances change by less than 0.04 Å, although V_{zz}(Pb) changes by about 20%. These indicate that the EFGs are a very sensitive probe of local structural changes. this is discussed further below in Sec. V A. The large changes in Pb EFGs seen here are consistent with the large changes observed in recent NMR ^{207}Pb spectra[25] as the Zr composition of PZT is varied, and the resulting Pb chemical shieldings change.

In Table II, the EFGs of Pb, Ti, and Zr in the *P*2*mm* and *P*1 structures are similar to those in the monoclinic symmetry with the same c/a value. V_{zz}(Zr) in rhombohedral *R*3*m*

TABLE II. Calculated EFGs (V_{zz} in units of 10^{22} V/m^2) for PZT 50/50 with imposed monoclinic *Cm*, triclinic *P*1, tetragonal *P*4*mm*, orthorhombic *P*2*mm*, and rhombohedral *R*3*m* symmetries. Note that in *P*1 and *P*2*mm* symmetries, the two O_2 and two O_4 atoms are not equivalent, while in *R*3*m* symmetry, atoms labeled O_1 and O_2 are equivalent (and similarly for oxygen atoms labeled O_3 and O_4).

	Cm						*P*1		*P*4*mm*		*P*2*mm*		*R*3*m*	
	$c/a=1.0$		$c/a=1.035$		$c/a=1.055$		$c/a=1.055$		$c/a=1.055$		$c/a=1.04$		$c/a=1.0$	
	V_{zz}	η	V_{zz}	η	V_{zz}	η	V_{zz}	η	V_{zz}	η	V_{zz}	η	V_{zz}	η
Pb_1	2.102	0.065	1.515	0.455	0.846	0.475	1.043	0.508	0.347	0	0.806	0.338	1.937	0
Pb_2	2.450	0.157	2.001	0.527	1.280	0.542	1.469	0.542	0.470	0	0.806	0.338	2.403	0
Zr	−0.972	0.159	−0.847	0.008	−0.750	0.017	−0.809	0.022	−0.685	0	−0.948	0.220	−0.393	0
Ti	0.507	0.866	0.462	0.445	0.372	0.173	0.373	0.247	0.376	0	0.422	0.545	−0.229	0
O_1	−0.126	0.077	0.121	0.666	0.146	0.157	0.137	0.255	0.152	0	−0.173	0.419	−0.125	0.088
O_2	0.220	0.954	0.163	0.966	0.149	0.922	0.147	0.967	0.149	0.944	−0.173	0.419	−0.125	0.088
O_2	0.220	0.954	0.163	0.966	0.149	0.922	0.147	0.959	0.149	0.944	−0.385	0.450	−0.125	0.088
O_3	−0.108	0.266	0.134	0.506	0.179	0.100	0.168	0.166	0.192	0	0.302	0.611	−0.144	0.434
O_4	0.170	0.758	0.238	0.488	0.256	0.405	0.248	0.419	0.270	0.380	−0.129	0.557	−0.144	0.434
O_4	0.170	0.758	0.238	0.488	0.256	0.405	0.247	0.426	0.270	0.380	−0.146	0.669	−0.144	0.434

TABLE III. Calculated EFGs (V_{zz} in units of 10^{22} V/m^2) for tetragonal $PbTiO_3$. All calculations are at the experimental volume. "Expt." indicates that both the experimental (Ref. 44) $c/a=1.0636$ and atomic positions (reduced coordinates u_i) were used. The other EFG results are obtained using the fully relaxed atomic positions at the indicated c/a.

	Expt. $c/a=1.0636$			$c/a=1.065$		
	u_i	V_{zz}	η	u_i	V_{zz}	η
Pb	0.0	0.361	0.0	0.0	0.472	0.0
Ti	0.549	−0.172	0.0	0.546	−0.097	0.0
O_1	0.117	0.061	0.0	0.122	0.111	0.0
O_2	0.620	0.109	0.697	0.626	0.125	0.638

PZT is much smaller than in all other [001] chemically stacked structures, but this EFG is in very good agreement with the V_{zz}(Zr) value of −0.356 (in units of 10^{22} V/m^2) in the antiferroelectric $PbZrO_3$ calculated by Johannes and Singh.[17] This indicates that the Zr EFG is sensitive only to the *B*-site ordering and less sensitive to the polarization and the strain. Compared to the EFG values for $PbTiO_3$ shown in Table III, V_{zz}(Ti) is significantly larger in PZT. There is also a sign change for both V_{zz}(Pb) and V_{zz}(Ti) in PZT compared to $PbTiO_3$, with the exception of rhombohedral PZT.

To help understand the structural dependence of the calculated EFGs, it is helpful to examine the orientation of the EFG principal axes eigenvectors. We first note that, by symmetry, one of the eigenvectors of the EFG tensors must be perpendicular to the *Cm* mirror plane. We label the corresponding eigenvalue $V_\perp$. The other two eigenvectors necessarily lie in the mirror plane. Of these two eigenvectors, the one with the larger dot product with the [001] unit vector (*c* axis) has its eigenvalue labeled V_c, and the other is labeled $V_\parallel$. In the following, we refer to $V_\perp$, $V_\parallel$, and V_c as "projected" EFG eigenvalues. The projected eigenvalues (rather than the conventionally defined parameters V_{zz} and η) are plotted in Figs. 5–7 for the cations and apex oxygen atoms. The projected eigenvalues are seen to approach the tetragonal *P*4*mm* values $V_{xx}=V_{yy}$ and V_{zz} as c/a increases. For Pb, Zr, and Ti, the projected eigenvalue V_c always equals V_{zz}, the conventional (largest magnitude) principal axes EFG eigenvalue. However, for the apex oxygens, $V_\parallel=V_{zz}$ for c/a less than about 1.03, while for larger c/a values, $V_c=V_{zz}$. This abrupt change in direction of the apex oxygens' V_{zz} eigenvector is due to polarization rotation. As c/a decreases from the largest values shown, the projected V_c eigenvalue for the apex-O atoms decreases as the BO_6 octahedra begin to rotate and shear from tetragonal symmetry. Similarly, for large c/a, while the system is nearly tetragonal, $V_\perp \simeq V_\parallel$, both being nearly equal to $V_{xx}=V_{yy}$ in *P*4*mm* symmetry. With decreasing c/a, $V_\perp$ becomes less negative, changing sign near $c/a \simeq 1.03$. At this point, the asymmetry parameter reaches it's maximum $\eta=1$, and the eigenvector associated with $V_\parallel$ becomes the largest eigenvalue $V_\parallel=V_{zz}$ as c/a further decreases. In Sec. V B below (see especially Fig. 17), octahedral shearing is shown to be a very sensitive indicator of the onset of polarization rotation.

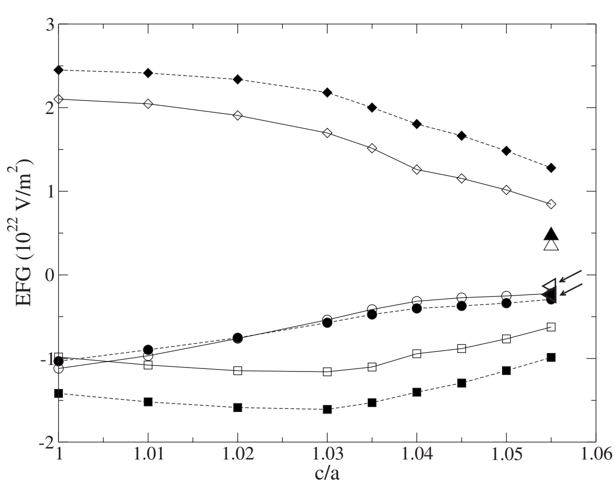

FIG. 5. Pb projected EFG eigenvalues (see text) vs c/a: circles label $V_\perp$, the EFG eigenvalue for the eigenvector that is perpendicular to the *Cm* mirror plane; diamonds label V_c, the EFG eigenvalue for the eigenvector that is approximately parallel to the *c* axis; squares label $V_\parallel$, the EFG eigenvalue for the remaining eigenvector. The large up triangles and left triangles at $c/a=1.055$, which are identified by arrows for clarity in some cases, represent the conventional EFG eigenvalues calculated in imposed *P*4*mm* symmetry: $V_{xx}=V_{yy}$ (left triangles) and V_{zz} (up triangles). All open symbols are for Pb_1, and filled symbols are for Pb_2.

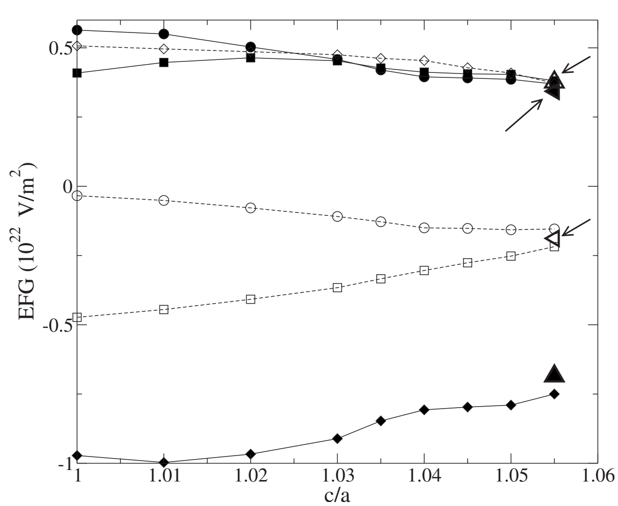

FIG. 6. Same as Fig. 5, but for Zr and Ti projected EFG eigenvalues (see text). All open symbols are for Ti, and filled symbols are for Zr.

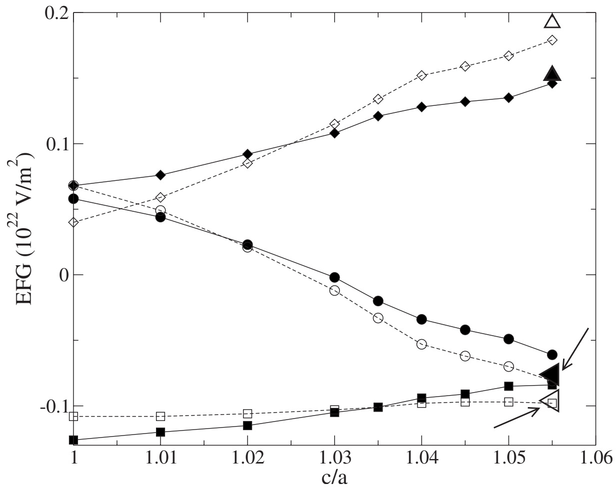

FIG. 7. Same as Fig. 5, but for the apex-O projected EFG eigenvalues (see text). All filled symbols are for O_1 (shortest B–O bond with Zr), and open symbols are for O_3 (shortest B–O bond with Ti).

Direct experimental measurement of the sign of the EFG eigenvalues is difficult to achieve and almost never available. However, it could be indirectly observed from measured NMR spectra. This is illustrated in the simulated NMR EFG powder spectra shown in Figs. 8–11 for monoclinic *Cm*. For each atom, the corresponding spectrum of tetragonal *P*4*mm* PZT (for $c/a=1.055$) is also shown for comparison. (NMR spectra for Pb are not shown, since the naturally occurring isotopes have no quadrupolar interaction.) The spectra are powder patterns of the central ($m=1/2 \leftrightarrow -1/2$) $\nu_{1/2}^{(2)}$ transition (see, for example, Refs. 10 and 31). The width of the spectrum is proportional to the square of the V_{zz}, while the splitting of the peaks is controlled by the value of η, with large η corresponding to small peak splitting.

In simulating these spectra, the values used for the quadrupole moments Q were -17.6, 30.2, and -2.558 fm^2 for

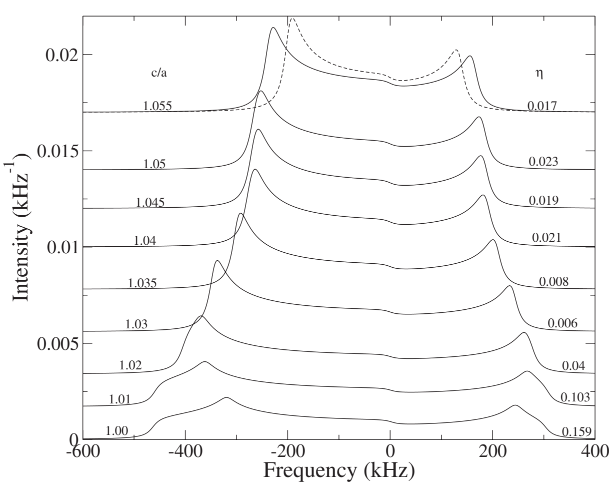

FIG. 8. ^{91}Zr calculated static central peak NMR powder spectrum in monoclinic *Cm* PZT. For comparison, the dotted curve shows the spectrum in tetragonal *P*4*mm* PZT with $c/a=1.055$. Numbers labeling the curves show the corresponding c/a and η values, as indicated. All simulated spectra are normalized to unit area.

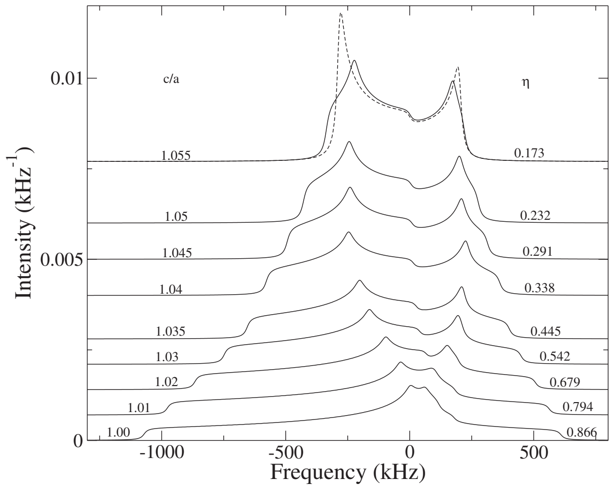

FIG. 9. ^{47}Ti static NMR powder spectrum in monoclinic *Cm* PZT. Dotted curve as in Fig. 8.

^{91}Zr, ^{47}Ti, and ^{17}O, respectively.[35] All these nuclear isotopes have spin $I=5/2$, and the powder patterns were calculated for an applied (high) field of $B=17.6$ T, which corresponds to Larmor frequencies of 70.0, 42.3, and 101.7 MHz for ^{91}Zr, ^{47}Ti, and ^{17}O, respectively. NMR experimental spectra are normally observed for the above isotopes, except for Ti, where both ^{47}Ti ($I=5/2$) and ^{49}Ti ($I=7/2$) have nearly overlapping spectra. These two isotopes have very similar magnetic moments, so the difference between their resonance frequencies is small: for example, it is only 9 kHz in a 14.1 T applied field. The Ti central transition thus shows overlapping spectra in the experiments,[36] and the relative EFG broadenings of ^{47}Ti and ^{49}Ti are $\Delta\nu^{47}/\Delta\nu^{49} \sim 3.44$. In our simulations, the spectra of the two Ti isotopes are, of course, completely separable, and only the spectra for ^{47}Ti are shown in Fig. 9.

The calculated NMR spectra of Ti, apex O_1 and O_3, and Ti coplanar O_4 atoms show the largest sensitivity to c/a. The spectra of the ferroelectrically inactive Zr and its equatorial O_2 atom show the least sensitivity. All spectra are seen to

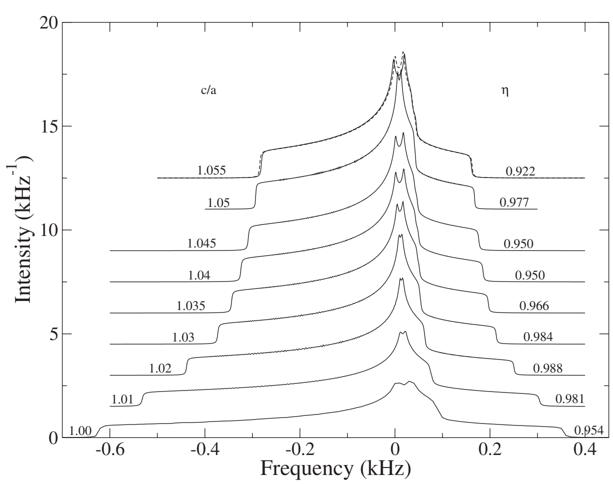

FIG. 10. ^{17}O static NMR powder spectrum for the O_2 atom (equatorial O approximately in the Zr plane). Dotted curve as in Fig. 8.

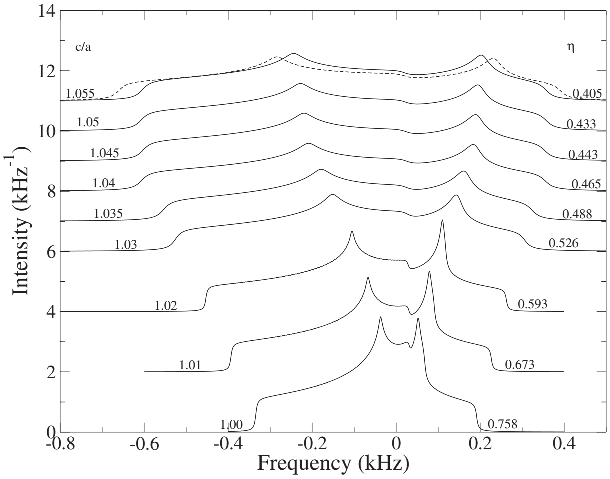

FIG. 11. ^{17}O static NMR powder spectrum for the O_4 atom (equatorial O approximately in the Ti plane). Dotted curve as in Fig. 8.

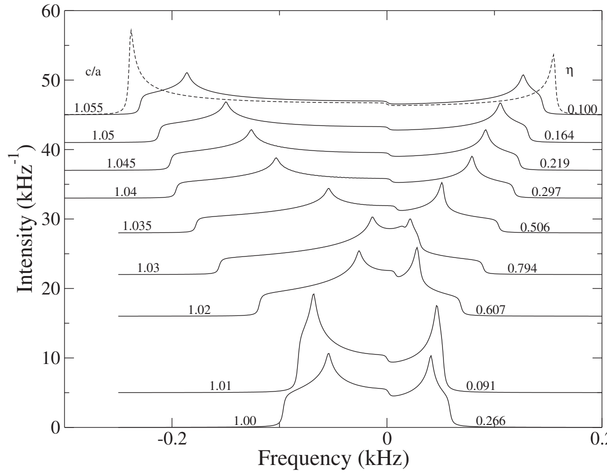

FIG. 13. ^{17}O static NMR powder spectrum for the apex O_3 atom (apex O nearest to Ti). Dotted curve as in Fig. 8.

approach the $P4mm$ spectra at the largest c/a values. The Ti spectra show a large decrease in width and an increase in peak splitting as c/a increases from 1.0 to 1.055. The spectra of the O_4 atom, which is coplanar with Ti, have splittings that follow a similar trend as for Ti, but the width displays an opposite trend to Ti, increasing as c/a increases. The apex oxygen spectra are also seen to be much narrower than the coplanar oxygens.

The apex-O simulation spectra seen in Figs. 12 and 13 reflect the abrupt switch in direction of the V_{zz} eigenvector, which occurs when $V_{\perp}=0$ near $c/a=1.03$ in Fig. 7. As mentioned, the asymmetry parameter reaches its maximum $\eta=1$ at this point, and this is evident in the near degeneracy of the two peaks at $c/a=1.03$ in Figs. 12 and 13. At this value of c/a, the polarization is beginning to rotate away from the [001] direction as c/a decreases. The apex-O EFG spectra are thus seen to be a very sensitive probe of structural changes associated with the onset of polarization rotation in PZT.

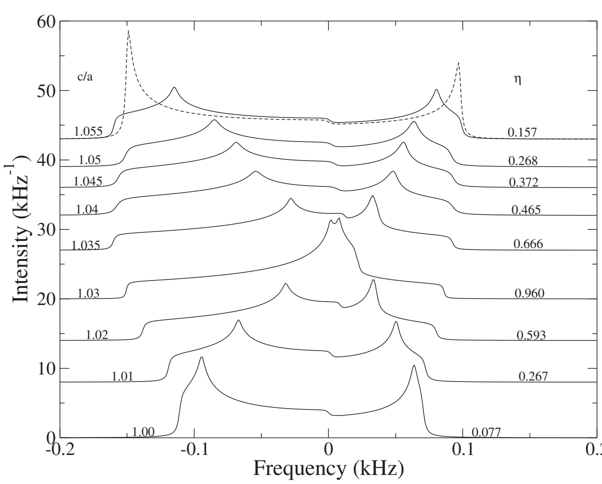

FIG. 12. ^{17}O static NMR powder spectrum for the apex O_1 atom (apex O nearest to Zr). Note the change in the frequency scale. Dotted curve as in Fig. 8.

V. DISCUSSION

Since the Pb atoms give a large contribution to the electric polarization, and since the Pb EFGs show considerable sensitivity to *B*-site ordering, strain, and imposed symmetry, the first section below presents a detailed analysis and discussion of the calculated Pb EFGs and compares these to a very limited number of non-NMR experimental measurements.

The second section discusses the structural dependence of the calculated EFGs of the Ti and O atoms and their sensitivity to the onset of polarization rotation. We also consider the recent suggestion by Baldwin *et al.*[25] of an anisotropy in the local structure of PZT solutions, based on their Ti and O NMR measurements.

A. Pb off-centering and lone-pair contributions to the electric field gradient

We first discuss the limited experimental data available for Pb EFGs. Pronounced changes in the EFGs of the Pb and O atoms are seen in Sec. IV as a function of polarization rotation and imposed symmetry. While the electric polarization lies essentially along [001] for $c/a \gtrsim 1.04$,[22] Figs. 3 and 4 show that the Cm monoclinic distortions (see Table I) result in $\eta(\mathrm{Pb}) \sim 0.5$ near $c/a=1.04$, rather than zero as required by $P4mm$ symmetry. Moreover, there is about an order of magnitude difference in $V_{zz}(\mathrm{Pb})$ between $P4mm$ and Cm imposed symmetries near $c/a=1.04$. NMR measurements cannot be used to determine Pb EFGs, since the naturally occurring isotopes have no quadrupole moment (nuclear spin $I \leq 1/2$). However, perturbed angular γ-γ correlation measurements, using metastable Pb isomers, can yield information about the Pb EFGs,[37–39] and they are a promising tool for investigating the striking structural sensitivity of Pb EFGs, which we predict.

Herzog *et al.*[37] reported measurements in ferroelectric $PbTiO_3$ using metastable ^{204m}Pb, which has a half-life of about an hour. ^{204m}Pb implantation energies of 70 keV were used. Troger *et al.*[38] implanted 60 keV ^{204m}Pb or ^{204m}Bi (half-life decay=11.2 h to ^{204m}Pb) in Cd metal, with subsequent annealing times of 0–10 min. Both ^{204m}Pb and ^{204m}Bi probes have the same intermediate ^{204m}Pb state with a half-life of 265 ns.[38,40] Herzog *et al.*[37] report $Q=0.68(15)$ b for the intermediate state, while the table of isotopes reports $Q=0.44(2)$ b.[40] In an unpublished report, Dietrich[41] also presented similar measurements using ^{204m}Pb implanted in $PbTiO_3$ and PZT 40/60.

In $PbTiO_3$, the experimentally measured $C_Q=eQV_{zz}/h=64.2(6)$ and 65.6(2) MHz, in Refs. 37 and 41, respectively, are in good agreement with each other. A comparison between theory and experiment depends on the value of the quadrupole moment Q of the ^{204m}Pb intermediate state. Using $Q=0.68(15)$ b of Herzog *et al.* and the calculated V_{zz}(Pb) for the experimental structure in Table III, we obtain $C_Q=70(15)$ MHz. Using $Q=0.44(2)$ b, we obtain $C_Q=45(2)$ MHz. Alternatively, using our calculated V_{zz}(Pb) and experimentally measured $C_Q=64.2(6)$ MHz of Herzog *et al.*, our LDA calculations would yield $Q=0.62(1)$ b. However, first-principles LAPW calculations for PbO were within 4% of the experimentally measured C_Q using $Q=0.44(2)$ b.[39] The 1974 measurement of Herzog *et al.*[37] of $C_Q=64.2(6)$ MHz is the only published value for $PbTiO_3$ of which we are aware. Structural damage and incomplete annealing are certainly possible at the large 70 keV ^{204m}Pb implantation energies used by Herzog *et al.* and also by Dietrich.[41]

In PZT 40/60, $C_Q(\mathrm{Pb})=128(5)$ MHz was measured, with $\eta(\mathrm{Pb})=0.04(9)$.[41] Our calculated values [we report values for $Q=0.44(2)$ b only, since results for other values of Q are related by a trivial scale factor] are $C_Q(\mathrm{Pb})=36-49$ MHz for Pb_1-Pb_2 in tetragonal $P4mm$. As seen in Fig. 3, these are characteristic for $P4mm$ imposed symmetry for the entire range of c/a. For monoclinic Cm symmetry with $c/a=1.045$, we obtain $C_Q(\mathrm{Pb})=123-177$ MHz. The calculated values for Cm symmetry are larger for smaller c/a, as seen in Fig. 3. For $P2mm$ symmetry, both Pb atoms are equivalent in our simulations, and we obtain for $c/a=1.04$ $C_Q(\mathrm{Pb})=86(4)$ MHz. As seen in Table II and Fig. 3, all symmetries except tetragonal $P4mm$ symmetry and Cm symmetry with $c/a=1.0$ have sizable values of η. Our calculations, which show large changes of V_{zz}(Pb) between $PbTiO_3$ and PZT 50/50 and between different imposed symmetries, are consistent with the limited available experimental data. Further experimental work to assess these predictions is desirable.

The large variations of Pb EFGs arise from the strong Pb-O covalency and differences in the Pb off centerings with respect to their nearest-neighbor O atoms. These differences are evident in Fig. 2 and Table I. Before discussing covalency effects, we first point out that the EFGs of the Pb atoms as well as those of the other cations are dominated by the contributions to the Coulomb potential arising from the charge distribution near the nucleus. This is shown in Table IV, which presents the EFGs calculated (i) using only the charge density inside the muffin-tin (MT) sphere and (ii) using only the charge density outside the MT. For example the internal EFG tensor component V_{zz} is given by[42]

TABLE IV. Electric field gradient contributions arising from the charge density inside and outside the muffin-tin (MT) spheres for monoclinic Cm PZT 50/50 with $c/a=1.035$. V_{zz} in units of 10^{22} V/m^2.

	Inside MT charges only		Outside MT charges only	
	V_{zz}	η	V_{zz}	η
Pb_1	1.515	0.455	−0.0014	0.500
Pb_2	2.000	0.526	−0.003	0.367
Zr	−0.845	0.008	−0.0027	0.519
Ti	0.455	0.442	0.007	0.671
O_1	0.217	0.327	−0.097	0.093
O_2	0.265	0.525	−0.102	0.196
O_3	0.242	0.248	−0.109	0.064
O_4	−0.206	0.777	−0.084	0.333

$$V_{zz}=\left[\frac{4\pi}{5}\right]^{1/2}\int_0^{R_{MT}}\frac{\rho_{20}(r)}{r^3}r^2dr, \tag{2}$$

where R_{MT} is the MT sphere radius and $\rho_{20}(r)$ is the ($L=2$, $M=0$) radial coefficient in the (real) spherical harmonic decomposition of the MT charge density in the EFG principal axis frame. For the cations, Table IV shows that external contributions to the EFGs are negligible compared to the internal ones, which are essentially equal to the total cation EFG (see Cm $c/a=1.035$ in Table II). For the O atoms in PZT, however, Table IV shows that the external contributions are much larger. The predominance of charge distributions near the nucleus was also noted by Wei and Zunger[42] in ordered $GaInP_2$. They found that 95% of the EFG in Eq. (2) arises from the electron charge distribution inside a small sphere with radius of $R=0.2$ Å. The cation EFGs in the present calculation also show predominant contributions coming from the charge distribution very close to the nuclei. As mentioned, this underscores the importance of an all-electron treatment of the electronic states near the nucleus.

To examine the effects of covalency on the Pb EFGs, Table V shows the calculated orbital decomposition of V_{zz}(Pb) and η(Pb) in PZT with imposed monoclinic Cm symmetry. The results were obtained by synthesizing the charge density using only the energy bands corresponding to the Pb($5d$), Pb($6s$), O($2s$), and O($2p$) valence states and to the Ti($3s,3p$) and Zr($4s,4p$) semicore contributions. Since V_{zz} and η refer to the eigenvalues of the EFG tensor, the contributions in the table cannot be directly summed and compared to the total EFG. (However, the contributions from different states to each component of the EFG tensor can be summed, and the sum yields the total EFG tensor.) Nevertheless, the eigenvalues in Table V are indicative of the relative magnitude of the contributions. Thus, for example, the contributions from the Ti($3s,3p$) and Zr($4s,4p$) semicore states are seen to be negligible. The Pb-O interaction dominates the Pb EFGs: both O $2s$ and $2p$ bands have large positive contributions to the EFGs in the monoclinic PZT, while the Pb $5d$ band gives large negative contributions. Moreover, the

TABLE V. Orbital decomposition of calculated Pb EFGs for monoclinic PZT with $c/a=1.035$. Contributions from bands with predominant Pb(5*d*), Pb(6*s*), O(2*s*), O(2*p*), Ti(3*s*), Ti(3*p*), Zr(4*s*), and Zr(4*p*) are shown. V_{zz} is in units of 10^{22} V/m^2.

	Pb 5*d*		Pb 6*s*	
	V_{zz}	η	V_{zz}	η
Pb_1	−2.167	0.494	0.103	0.131
Pb_2	−2.232	0.300	0.111	0.114
	O 2*s*		O 2*p*	
	V_{zz}	η	V_{zz}	η
Pb_1	2.185	0.506	1.430	0.494
Pb_2	2.273	0.325	1.909	0.554
	Ti 3*s*		Ti 3*p*	
	V_{zz}	η	V_{zz}	η
Pb_1	0	0.039	0	0.190
Pb_2	0	0.019	0	0.411
	Zr 4*s*		Zr 4*p*	
	V_{zz}	η	V_{zz}	η
Pb_1	0	0.298	0.005	0.438
Pb_2	0	0.536	−0.001	0.984

O 2*s* and Pb 5*d* contributions to V_{zz}(Pb) and η(Pb) are seen to nearly cancel. This is verified by adding the O 2*s* and Pb 5*d* EFG tensors and then obtaining the eigenvalues. Since the Pb 6*s* contribution is small in Table V, the dominant contribution to the Pb EFGs is seen to come from the O 2*p* states.

This can be understood in the context of the lone-pair picture of the Pb 6*s* orbital. In an on-site atomic orbital picture, the lone pair can be viewed as arising from the hybridization of the Pb 6*s* and unoccupied 6*p* orbital. A recent study by Payne *et al.*[43] instead attributes it to the hybridization of the Pb 6*s* lone pair and the O 2*p* electrons. The two pictures are not necessarily incompatible, since the states that are identified as predominantly O 2*p* can have Pb 6*p* character near the Pb nucleus. The calculated Pb 5*d* and O 2*s* states are more than 10 eV lower than the Fermi energy and, as noted above, give a combined contribution to the to the Pb EFG, which is negligible. The closed-shell Pb 6*s* is also seen to give a negligible contribution. Significant Pb 6*s*-O 2*p* hybridization, however, leads to mixing in of some Pb 6*p* character within an on-site atomic orbital decomposition, resulting in the familiar lone-pair picture. This shows up as the large O 2*p* contribution in Table V.

B. Ti and O calculated EFGs and possible structural anisotropy in $PbZr_{1-x}Ti_xO_3$

Recently, Baldwin *et al.*[25] presented an NMR solid-state study of $PbZr_{1-x}Ti_xO_3$ solid-solution series as a function of *x*. In $PbTiO_3$ ($x=1$), they observed two distinct ^{17}O peaks, which were unambiguously identified with the axial (650 ppm) and coplanar (450 ppm) O atoms. The evolution of these two peaks with increasing Zr concentration was quite different. While the coplanar-O peak persisted down to $x=0.25$ with little change in frequency, the apex-O peak disappeared for $x<0.75$. They interpreted their measurements as indicating that Ti-O-Ti chains involving the Ti coplanar-O atoms (i.e., chains along the *x* and *y* directions, perpendicular to the *c* axis) were preserved down to $x=0.25$, while Ti-O-Ti chains involving the apex-O atoms (i.e., chains along the *c* axis) were absent for $x<0.75$. Their Ti NMR spectra, however, showed little variation over this concentration range, and this is discussed further below. Based on the above observations, they concluded that there is a local structural anisotropy in PZT. Our simulation model based on [001]1:1 *B* site $x=1/2$ chemical ordering retains Ti-O-Ti chains in the [100] and [010] directions, but not along [001], where only Zr-O-Ti chains exist. We can thus examine the interpretation of Baldwin *et al.* using the calculated EFGs for this structure. Before doing this, we first discuss the calculated Ti EFG's in some detail.

For $PbTiO_3$, the present Ti calculated EFGs are in good agreement with experiment and with other calculations. Our calculated V_{zz}(Ti), using the $PbTiO_3$ structure given in the paper of Padro *et al.*,[44] is in excellent agreement with their WIEN97 LAPW calculation as well as their NMR measurements. We note, however, that the calculated Ti EFGs are very sensitive to small variations in the internal structural coordinates. For example, the $PbTiO_3$ experimental structures given by Sharing and Pepinsky[45] and Glazer and Mabud[46] differ by only 0.023 Å in the Ti-O(apex) distance. The corresponding calculated V_{zz}(Ti) are −0.184 and −0.115 (10^{22} V/m^2), respectively. This difference equates to a factor of $\simeq$2.5 in the corresponding NMR central peak quadrupolar powder linewidths. In this regard, we note that the reported experimental structure of the ^{17}O-doped $PbTiO_3$ sample used by Baldwin *et al.*[25] appears to be anomalous, yielding a Ti-O(apex) distance of 2.112(5) Å, which is much larger than the distance of 1.78 Å reported by Sharing and Pepinsky[45] and Glazer and Mabud.[46] It is not clear which structure was used in their LAPW calculations.

For $PbZr_{1-x}TixO_3$, the measured Ti spectra reported by Baldwin *et al.*[25] show very similar powder spectra for $x=1$ (pure $PbTiO_3$), $x=0.75$, and $x=0.0.5$ (see their Fig. 5). This indicates that the Ti EFGs are similar in all their samples over this concentration range. This is not consistent with our calculated results. Figure 14 shows our calculated $x=1/2$ Ti quadrupole central peak static powder spectra for monoclinic, tetragonal, orthorhombic *P*2*mm*, and rhombohedral PZT and tetragonal $PbTiO_3$. All, but the rhombohedral structure, have [001]1:1 *B*-site ordering. The spectra are all seen to be much broader than that of $PbTiO_3$.

To assess this discrepancy in PZT Ti EFGs between experiment and theory, we examine the structural sensitivity of the calculated Ti EFGs in more detail. We first show, for PZT 50/50, the volume dependence of the calculated V_{zz}(Ti) in Fig. 15 for imposed tetragonal (with fixed $c/a=1.035$) and for rhombohedral symmetries. The tetragonal [001]1:1 *B*-site

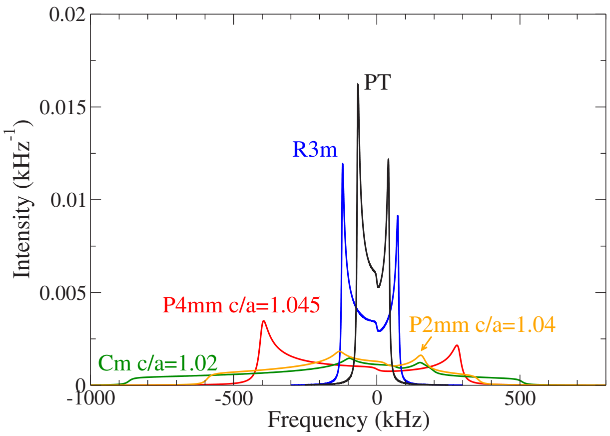

FIG. 14. (Color online) Calculated NMR quadrupole powder spectra of ^{49}Ti: pure $PbTiO_3$ calculated at the experimental structure (black), PZT [001]1:1 tetragonal c/a=1.045 (red), PZT [001]1:1 monoclinic c/a=1.02 (green), PZT [111]1:1 rhombohedral (blue), and PZT [001]1:1 orthorhombic *P2mm* c/a=1.04 (orange).

ordered structure shows little sensitivity, while the rhombohedral [111]1:1 *B*-site ordered structure shows greater variation. Sensitivity to longitudinal and shear distortions of the TiO_6 octahedra is examined next.

The longitudinal strain $|\alpha|$ of the TiO_6 octahedron[44,47] is defined as

$$|\alpha| = \sum_{i}^{6} \left| \ln\left(\frac{l_i}{l_u}\right) \right|, \quad (3)$$

where l_i is the Ti-O bond length of the distorted TiO_6 octahedron and l_u is the undistorted bond length corresponding to the ideal perovskite structure. Figure 16 shows the calculated PZT Ti V_{zz} as a function of $|\alpha|$ in imposed monoclinic *Cm* and tetragonal *P4mm* symmetries. At the largest c/a values, the Ti V_{zz} have similar values in both monoclinic *Cm* and tetragonal *P4mm* imposed symmetries, although the longitudinal strains $|\alpha|$ differ by about 25% at the largest c/a =1.055 shown. Both symmetries show a nearly linear variation, but relaxing the *P4mm* symmetry greatly reduces the slope. Although the onset of polarization rotation in monoclinic *Cm* symmetry starts at $c/a \simeq 1.035$ as c/a reduced,[22] there is no indication of this in Fig. 16.

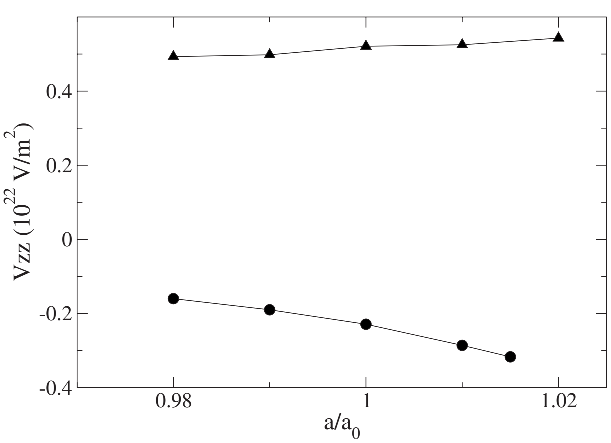

FIG. 15. Volume dependence of the calculated PZT 50/50 V_{zz}(Ti). Circles indicate rhombohedral *R3m* imposed symmetry. Triangles indicate imposed tetragonal *P4mm* symmetry with c/a =1.035 PZT. The lattice parameter a_0 corresponds to the experimental volume.

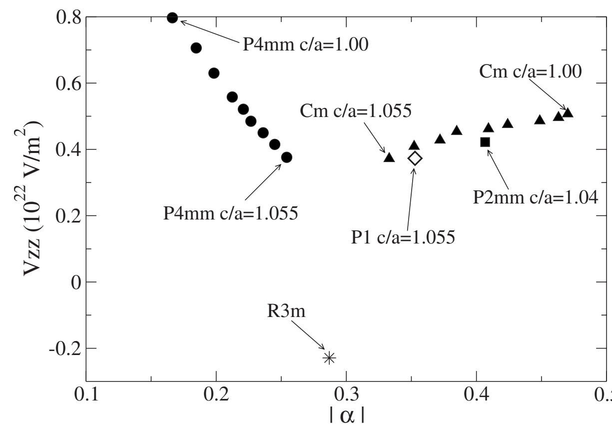

FIG. 16. Longitudinal strain ($|\alpha|$, see text) dependence of the calculated PZT 50/50 V_{zz}(Ti). for different imposed symmetries: tetragonal *P4mm* (circles), orthorhombic *P2mm* (square), monoclinic *Cm* (triangles), triclinic *P*1 (diamond), and rhombohedral *R*3*m* (star).

By contrast, the onset of polarization rotation in *Cm* symmetry strongly correlates with the shearing of the TiO_6 octahedra. One measure of the shear strain is the distortion index[44,47] (DI)

$$\mathrm{DI} = \frac{\sum_{i=1}^{12} |\theta_i - 90°|}{\sum_{i=1}^{12} 90°}, \quad (4)$$

where there are 12 O-Ti-O angles of 90° in the unsheared TiO_6 octahedra, while the θ_i are the angles in the distorted octahedra. Figure 17 shows the dependence of V_{zz}(Ti) on DI.

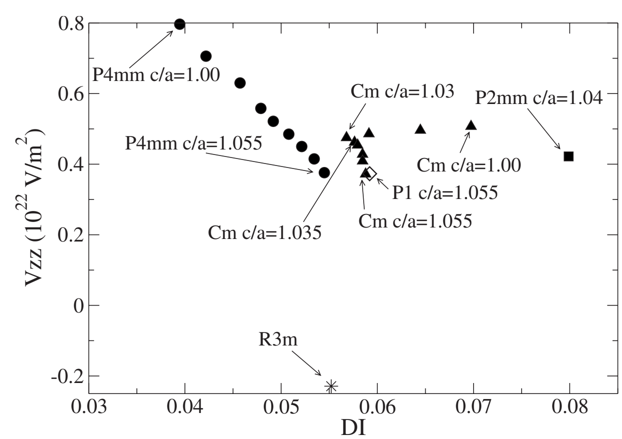

FIG. 17. Shear strain [distortion index (DI), see text] dependence of the calculated PZT 50/50 V_{zz}(Ti) for different imposed symmetries. Same legends as in Fig. 16.

Note that DI is nonzero in tetragonal PZT due to the off centering of the Ti atoms. As c/a increases in tetragonal PZT, the Ti off centering increases. For imposed *Cm* symmetry, there is a sharp break in the slope at $c/a=1.03$. This is caused by the abruptly larger shearing of the octahedra when the polarization rotates away from the [001] direction with decreasing c/a. For c/a values larger than 1.03, the variation of V_{zz}(Ti) with DI is similar to that in tetragonal symmetry. For smaller values of c/a, DI in *Cm* symmetry rapidly increases, although V_{zz} shows little change.

We now discuss the discrepancy between the experimentally measured PZT 50/50 Ti spectra and the calculated spectra in Fig. 14. While the experimental spectra indicate similar η(Ti)$\simeq 0$ and similar values of V_{zz}(Ti) for 0%–75% Zr compositions,[25] this is not the case for the calculated spectra. The EFGs shown in Table II and Figs. 16 and 17 show that the calculated V_{zz}(Ti) in PZT 50/50 are all much larger than in $PbTiO_3$. If we take the *Cm* [001]1:1 *B*-site ordered calculated V_{zz}'s in the range $c/a<1.03$ (Figs. 16 and 17) as representative of PZT 50/50, these values are about 2.3 times larger than that for $PbTiO_3$, corresponding to a factor of about 5 times greater powder linewidths. Moreover, in *Cm* symmetry, the EFG asymmetry η(Ti) increases with decreasing c/a, which also tends to increase the linewidth, as is evident from Fig. 14.

One explanation is that the discrepancy results from the limitations of the present simulation cells, which are all based on two perovskite formula units, in modeling the disordered structure of PZT 50/50. However, the good agreement of the calculated pair distribution functions (PDF) with the experimental PDFs in Fig. 2 indicates that the nearest-neighbor atomic structure is reasonably well reproduced. Moreover, the experimental NMR Ti spectra themselves suggest that only the nearest-neighbor structure near the Ti atoms is important and that the local Ti environment changes little over the 0%–75% Zr composition range. Specifically, this would indicate (1) that the Ti EFG is relatively insensitive to the chemical species occupying the nearest-neighbor *B* sites and (2) that the TiO_6 octahedra are only slightly modified compared to $PbTiO_3$. If that is the case, however, at least one of our PZT 50/50 simulations for both [001]1:1 and [111]1:1 *B*-site ordering, for various c/a values and symmetries, might be expected to closely represent the Ti local atomistic structure. However, only the PZT 50/50 [111]1:1 *B*-site ordered *R*3*m* rhombohedral model has η(Ti)$=0$ while at the same time having a V_{zz}(Ti) at least close in magnitude to that of $PbTiO_3$, *R*3*m* V_{zz}(Ti) being only 33% larger. As seen in Fig. 1, the experimental PDFs for rhombohedral *R*3*c* 40% Ti are quite similar to the experimental PDF of monoclinic *Cm* 48% Ti, while both of these show somewhat larger differences compared to the experimental PDF of *P*4*mm* 60% Ti. This is also evident in the calculated PDFs for PZT 50/50 in Fig. 2. However, in the *R*3*m* structure, which has a rocksalt-like *B*-site ordering, there are no intact Ti-O-Ti chains. We return to this point further below.

Another possible explanation for the experimentally observed lack of structural sensitivity of the NMR Ti spectra is that the PZT spectra are motionally narrowed. Evidence of motional narrowing in NMR quadrupole Ti spectra was recently reported in single-crystal cubic phases of the related perovskites $BaTiO_3$ and $SrTiO_3$.[48] These were interpreted as showing the mixed order-disorder and displacive character of the ferroelectric transition. The motional narrowing was interpreted as arising from a fast motion between eight nearly degenerate [111] off centerings, with a slight bias, on a slower time scale, toward a local tetragonal polarization along a cubic direction. In PZT, motional narrowing would be possible if there were several local atomistic structures which were energetically nearly degenerate. The relative ease of polarization rotation, which is responsible for the high piezoelectric constants in PZT and PMN-PT, reflects just such a soft energy landscape. For example, the energies of the PZT *Cm* $c/a=1.02$ and the *P*4*mm* $c/a=1.045$ structures differ only by about 1 mRy/perovskite unit.

We can now evaluate the suggestion by Baldwin *et al.*[25] of an anisotropy in the local structure of PZT solid solutions. Their interpretation is based on (1) very similar Ti NMR spectra for 0%–75% Zr concentration and (2) the disappearance of one of the two ^{17}O peaks (observed in pure $PbTiO_3$) for Zr compositions as small as $\simeq$25%. Due to the small ^{17}O quadrupole moment and relatively small EFGs, the observed ^{17}O lines are very narrow. (This is also evident in the small widths of the simulated O spectra in Figs. 10–13 compared to that of the other atoms.) These peaks are located at about 650 and 450 ppm (referenced to liquid water). Since the intensity of the 450 ppm peak is twice that of the 650 ppm peak, the 450 ppm peak was assigned to the O equatorial site, and the 650 ppm peak was assigned to the O apex site. The $\simeq$200 ppm difference is due to different chemical shieldings at the apex and equatorial sites (EFG central peak centroid shifts are negligible due to the small magnitudes of O EFGs). The disappearance of the 650 ppm peak with the addition of small concentrations of Zr atoms was interpreted as being due to the elimination of Ti-O-Ti chains along the z axis (polar axis), while the persistence of the 450 ppm peak up to about 75% Zr was interpreted as reflecting the presence of Ti-O-Ti chains along the x and y axes. While the calculation of chemical shielding is beyond the scope of the present work, we can examine the structural sensitivity of V_{zz}(O) and η(O) to infer information about changes in the O-site local environments. As can be seen in Figs. 3, 4, 7, and 10–13, V_{zz}(O) for the O_2 and O_4 equatorial atoms show little change with c/a in imposed *Cm* symmetry. The η(O) for the O_4 equatorial atom (roughly coplanar with Ti) decreases with increasing c/a, while the O_2 atom (roughly coplanar with Zr) shows little change. By contrast, the apex O_1 and O_3 atoms show much larger changes in V_{zz}(O) and η(O). This is most clearly seen in Figs. 7, 12, and 13. Thus, the calculated EFGs for the apex-O atom show considerable sensitivity to their local environment. Assuming that significant chemical shielding variations accompany the large EFG changes, this suggests that the introduction of Zr is likely to more strongly affect the apex O, which is consistent with the measurements of Baldwin *et al.*[25] This interpretation would favor a structure similar to our PZT 50/50 [001]1:1 model. As we have seen, however, the Ti EFGs yield central peak NMR powder patterns, which are much wider than observed, unless motional narrowing is invoked.

The persistence of the 450 ppm peak may not require, however, the persistence of Ti-O-Ti chains in the x and y directions. In $PbTiO_3$, the Ti-O-Ti x and y chains have equal $B-$O bond lengths, while the z chains have alternating short and long $B-$O bond lengths. In PZT 50/50, with either [001]1:1 or [111]1:1 order, there are still $B-$O bond lengths roughly equal to those in the Ti-O-Ti x and y chains. The 450 ppm peak could be associated with these. The disappearance of the 650 ppm peak could be accounted for if large changes in chemical shielding accompany the large structural dependence of the apex-O EFGs found in the present calculations. To explain the observed insensitivity of the Ti NMR spectra over the large PZT composition range, it is possible that, for Zr concentrations greater than about 40%, the local Ti structure is similar, on average, to that of our [111]1:1 ordering model. Indeed, this structure has the lowest energy of all the structures we have examined. Moreover, the experimental and calculated PDF curves in Figs. 1 and 2 suggest that the rhombohedral $R3m$ and Cm nearest-neighbor arrangements are quite similar. V_{zz}(Ti) in local $R3m$ symmetry is at least close to that in $PbTiO_3$ for both and with η(Ti) $=0$. A reduction in the effective volume of the TiO_6 octahedra (see Fig. 15) or some motional narrowing could reduce the V_{zz}(Ti) in local $R3m$ symmetry to that of $PbTiO_3$. In this scenario, there are no Ti-O-Ti chains, and there is no structural anisotropy in PZT.

There are thus several possible interpretations of the NMR measurements of Baldwin *et al.*[25] Their interpretation of a structural anisotropy in PZT would seem to rule out local $R3m$ [111]1:1 B-site ordering, since no Ti-O chains are present in the $R3m$ structure. This is inconsistent with the present Ti EFG calculations, which yield too large Ti EFGs and nonzero η's for all other Ti local structures in a static structural model. If motional narrowing of the Ti EFGs were present, however, this could resolve the discrepancy with the present calculations. Alternatively, an average local $R3m$ [111]1:1 B-site ordering, perhaps accompanied by less pronounced motional narrowing, would also be consistent with the present calculations, without invoking any static structural anisotropy in PZT. In this case, as mentioned, the persistence of the 450 ppm NMR peak could be accounted for by the presence, at all compositions, of Ti-O bond lengths similar to that of the coplanar-O atoms in $PbTiO_3$. The disappearance of the 650 ppm peak could be due to large structural dependence of the apex-O chemical shielding, paralleling the large structural dependence of the calculated apex-O EFGs.

VI. CONCLUSIONS

We have presented first-principles calculations of electric field gradients for $PbTiO_3$ and structural models of $Pb(Zr_{1/2}Ti_{1/2})O_3$, as a function of chemical ordering, applied strain, and imposed symmetry. The relaxed structural models yield pair distribution functions in good agreement with experiment. The calculations show large changes of the EFGs as the electric polarization rotates between the tetragonal and monoclinic structures. The onset of polarization rotation in Cm symmetry strongly correlates with the shearing of the TiO_6 octahedra, and there is a sharp change in slope in plots of Ti EFGs vs octahedral distortion index. Results for the oxygen EFGs are consistent with a greater sensitivity of the apex oxygen chemical shifts to the local environment compared to the equatorial oxygen atoms. This is qualitatively in agreement with recent ^{17}O nuclear magnetic resonance measurements. The calculated Ti EFGs are considerably larger than those deduced from the NMR measurements, which show little change in the Ti spectra with Zr concentration. Our calculated results were interpreted in light of a suggested structural anisotropy in PZT solid solutions, inferred from the NMR measurements. This was discussed in terms of static and dynamic local structural models of PZT.

ACKNOWLEDGMENTS

Support from ONR Grants No. N000140110365 and No. N000140510055 is acknowledged. Calculations were performed at the Center for Piezoelectrics by Design. We are grateful to W. Dmowski for making available numerical data from Ref. 7. We would like to thank R. Vold and G. Hoatson for useful discussions, and also thank R. Vold for making available his powder pattern computer program.

*hxkrak@wm.edu

[1] K. Uchino, *Piezoelectric Actuators and Ultrasonic Motors* (Kluwer Academic, Dordrecht, 1996).

[2] L. E. Cross, Ferroelectrics **151**, 305 (1994).

[3] R. E. Newnham, NIST Spec. Publ. **804**, 39 (1996).

[4] S.-E. Park and T. R. Shrout, J. Appl. Phys. **82**, 1804 (1997).

[5] G. A. Samara, Solid State Phys. **56**, 239 (2001).

[6] G. A. Samara, J. Phys.: Condens. Matter **15**, R367 (2003).

[7] W. Dmowski, T. Egami, L. Farber, and P. K. Davies, in *Fundamental Physics of Ferroelectrics*, edited by H. Krakauer, AIP Conf. Proc. No. 582 (AIP, New York, 2001), p. 33. We are grateful to W. Dmowski for making available numerical data corresponding to Figs. 4 and 5 in this paper.

[8] G. L. Hoatson, D. H. Zhou, F. Fayon, D. Massiot, and R. L. Vold, Phys. Rev. B **66**, 224103 (2002).

[9] B. Zalar, V. V. Laguta, and R. Blinc, Phys. Rev. Lett. **90**, 037601 (2003).

[10] J. F. Baugher, P. C. Taylor, T. Oja, and P. J. Bray, J. Chem. Phys. **50**, 4914 (1969).

[11] P. Blaha, K. Schwarz, and P. Herzig, Phys. Rev. Lett. **54**, 1192 (1985).

[12] Y. P. Blaha, K. Schwarz, and P. H. Dederichs, Phys. Rev. B **37**, 2792 (1988).

[13] P. Blaha, K. Schwarz, W. Faber, and J. Luitz, Hyperfine Interact. **126**, 389 (2000).

[14] P. Blaha, J. Phys.: Condens. Matter **3**, 9381 (1991).

[15] K. Schwarz, C. Ambrosch-Draxl, and P. Blaha, Phys. Rev. B **42**, 2051 (1990).

[16] D. J. Singh, Ferroelectrics **153**, 183 (1994).
[17] M. D. Johannes and D. J. Singh, Phys. Rev. B **71**, 212101 (2005).
[18] H. M. Petrilli, P. E. Blochl, P. Blaha, and K. Schwarz, Phys. Rev. B **57**, 14690 (1998).
[19] B. Noheda, D. E. Cox, G. Sharing, J. A. Gonzalo, L. E. Cross, and S.-E. Park, Appl. Phys. Lett. **74**, 2059 (1999).
[20] H. Fu and R. Cohen, Nature (London) **403**, 281 (2000).
[21] L. Bellaiche, A. Garcia, and D. Vanderbilt, Phys. Rev. Lett. **84**, 5427 (2000).
[22] Z. Wu and H. Krakauer, Phys. Rev. B **68**, 014112 (2003).
[23] B. Noheda, D. E. Cox, G. Sharing, S.-E. Park, L. E. Cross, and Z. Zhong, Phys. Rev. Lett. **86**, 3891 (2001).
[24] D. Vanderbilt and M. H. Cohen, Phys. Rev. B **63**, 094108 (2001).
[25] A. Baldwin, P. A. Thomas, and R. Dupree, J. Phys.: Condens. Matter **17**, 7159 (2005).
[26] D. Singh, *Planewaves, Pseudopotentials and the LAPW Method* (Kluwer Academic, Dordrecht, 1994).
[27] L. Hedin and B. I. Lundqvist, J. Phys. C **4**, 2064 (1971).
[28] H. J. Monkhorst and J. D. Pack, Phys. Rev. B **13**, 5188 (1976).
[29] J. Ehmann and M. Fahnle, Phys. Rev. B **55**, 7478 (1997).
[30] R. Sternheimer, Phys. Rev. **84**, 244 (1951).
[31] M. H. Cohen and F. Reif, Solid State Phys. **5**, 321 (1957).
[32] Calculations of hyperfine spectra and powder spectra were performed using a computer program provided by R. Vold.
[33] B. Noheda, J. A. Gonzalo, L. E. Cross, R. Guo, S.-E. Park, D. E. Cox, and G. Sharing, Phys. Rev. B **61**, 8687 (2000).
[34] T. Proffen and S. J. L. Billinge, J. Appl. Crystallogr. **32**, 572 (1999).
[35] R. K. Harris, E. D. Becker, S. D. Menezes, R. Goodfellow, and P. Granger, Pure Appl. Chem. **73**, 1795 (2001).
[36] D. Padro, A. P. Howes, M. E. Smith, and R. Dupree, Solid State Nucl. Magn. Reson. **15**, 231 (2000).
[37] P. Herzog, B. Klemme, and G. Schaefer, Z. Phys. **269**, 265 (1974).
[38] ISOLDE Collaboration, W. Troeger *et al.*, Z. Naturforsch., A: Phys. Sci. **57a**, 586 (2002).
[39] S. Friedemann, F. Heinrich, H. Haas, and W. Troeger, Hyperfine Interact. **159**, 313 (2004).
[40] R. B. Firestone, V. S. Shirley, S. Y. F. C. C. M. Baglin, and J. Zipkin, *Table of Isotopes*, 8th ed. (Wiley, New York, 1999).
[41] M. Dietrich (private communication); talk presented at the ISOLDE/CERN Physics Workshop, Geneva, Switzerland, 15–17 December 2003 (unpublished); http://isolde.web.cern.ch/ISOLDE/Workshop2003/workshop2003.htm; ν_Q in this reference is equal to C_Q defined in Appendix A.
[42] S. Wei and A. Zunger, J. Chem. Phys. **107**, 1931 (1997).
[43] D. J. Payne, R. G. Egdell, A. Walsh, G. W. Watson, J. Guo, P. A. Glans, T. Learmonth, and K. E. Smith, Phys. Rev. Lett. **96**, 157403 (2006).
[44] D. Padro, V. Jennings, M. E. Smith, R. Hoppe, P. A. Thomas, and R. Dupree, J. Phys. Chem. B **106**, 13176 (2002).
[45] G. Sharing and R. Pepinsky, Phys. Rev. **97**, 1179 (1955).
[46] A. M. Glazer and S. A. Mabud, Acta Crystallogr., Sect. B: Struct. Crystallogr. Cryst. Chem. **34**, 1065 (1978).
[47] W. H. Baur, Acta Crystallogr., Sect. B: Struct. Crystallogr. Cryst. Chem. **30**, 1195 (1974).
[48] B. Zalar, A. Lebar, J. Seliger, R. Blinc, V. V. Laguta, and M. Itoh, Phys. Rev. B **71**, 064107 (2005).